A metal-free ORR/OER bifunctional electrocatalyst derived from metal-organic frameworks for rechargeable Zn-Air…

Article · October 2016

DOI: 10.1016/j.carbon.2016.10.046

9 authors, including:

Zhigang Hu
National University of Singapore
30 PUBLICATIONS **348** CITATIONS
SEE PROFILE

Shiliu Yang
Jiangsu University
28 PUBLICATIONS **571** CITATIONS
SEE PROFILE

Jim Yang Lee
National University of Singapore
326 PUBLICATIONS **19,227** CITATIONS
SEE PROFILE

Carbon 111 (2017) 641–650

Contents lists available at ScienceDirect

Carbon

journal homepage: www.elsevier.com/locate/carbon

A metal-free ORR/OER bifunctional electrocatalyst derived from metal-organic frameworks for rechargeable Zn-Air batteries

Yuhong Qian [a], Zhigang Hu [a], Xiaoming Ge [b], Shiliu Yang [a], Yongwu Peng [a], Zixi Kang [a], Zhaolin Liu [b], Jim Yang Lee [a], Dan Zhao [a, *]

[a] Department of Chemical & Biomolecular Engineering, National University of Singapore, 4 Engineering Drive 4, 117585, Singapore
[b] Institute of Materials Research and Engineering (IMRE), A*STAR (Agency for Science, Technology and Research), Innovis, 2 Fusionopolis Way, 138634, Singapore

ARTICLE INFO

Article history:
Received 26 July 2016
Received in revised form
15 October 2016
Accepted 19 October 2016
Available online 19 October 2016

ABSTRACT

Rechargeable Zn-air batteries are under intensive studies because of their high-energy density, low cost, and safety. However, their wide application is prevented by several remaining technical issues, one of which is the lack of suitable bifunctional cathodic catalysts for oxygen reduction reaction (ORR) during discharging and oxygen evolution reaction (OER) during charging. Due to low material cost and wide distribution, carbon-based materials may serve as promising electrocatalysts, while doping heteroatoms such as nitrogen or boron can effectively enhance their catalytic activity. Herein, we pyrolyze a metal-organic framework containing Zn, N, and B as the precursor to synthesize dual-doped and metal-free porous carbon materials as efficient ORR/OER bifunctional electrocatalysts. The surface area of obtained carbon materials can be greatly enhanced by pyrolysis under H_2-containing atmosphere. In addition, N and B are evenly distributed within the carbon materials due to the crystalline MOF precursor. The resultant carbon materials exhibit high ORR and OER catalytic activities in both half-cell and single-cell battery measurements. Our study has demonstrated for the first time that MOFs can be used as precursors to synthesize metal-free ORR/OER bifunctional cathodic electrocatalysts with great potential in rechargeable Zn-air batteries.

1. Introduction

Battery technology has been attracting great attention recently due to its high efficiency, portability, and flexibility toward various energy demanding applications [1]. Among all the battery systems, rechargeable Zn-air batteries have experienced fast development because of their safety, easy production, and relatively high energy storage density [2,3]. In addition, the feature of rechargeability makes them more environmentally benign than the traditional dry batteries [4]. However, there are still several technical issues that need to be solved before their large-scale application, one of which is the slow kinetics of oxygen reduction reaction (ORR) during discharging and oxygen evolution reaction (OER) during charging at the cathodes [5]. For example, the exchange current density of ORR at cathodes is several orders lower than that of the oxidation reaction at anodes [6]. In addition, OER is critical to rechargeable Zn-air batteries in terms of recharge rate and voltage efficiency, which is however typically less than 60% in current systems [3]. Therefore, it is highly desirable to develop bifunctional electrocatalysts for both ORR and OER to speed up the electrochemical reactions and increase recharge rate as well as voltage efficiency of rechargeable Zn-air batteries. Platinum (Pt) is considered to be the most efficient ORR catalyst, but its high cost, easily-poisoned nature, and low durability hinder its wide application. Ruthenium (IV) oxide (RuO_2) is regarded as the most suitable OER catalyst [7], which however is limited by its scarcity and instability in alkaline solutions used in Zn-air batteries [8]. Compromised design of air cathodes have been proposed based on double-layer structures with two catalysts mixed together for both ORR and OER reactions, but at the cost of complexity and system stability [9]. Given the above concerns, a single cathodic catalyst with both ORR and OER activity would be the most efficient and cost-effective solution for rechargeable Zn-air batteries.

Porous materials loaded with transition metals have been extensively studied as ORR/OER catalysts [10–14], but they are

* Corresponding author.
E-mail address: chezhao@nus.edu.sg (D. Zhao).

http://dx.doi.org/10.1016/j.carbon.2016.10.046
0008-6223/

challenged by metal particle agglomeration and leaching after long term usage [15]. Due to the low material cost and wide distribution, carbon materials such as multi-layered graphene, carbon nanotube, and pyrolyzed polymers have been widely studied as electrocatalysts for ORR and OER [16–22]. Compared to loaded catalysts, metal-free carbon materials do not have the problems of particle agglomeration and leaching, thus may exhibit better stability during long term usage. In addition, it has been proven that doping carbon materials with one or several types of heteroatoms (*e.g.*, N, P, S, B, *etc.*) is beneficial for their electrocatalytic performance. For example, Lai et al. systematically studied the roles of different types of doped N in ORR electrocatalysts and found that quaternary N and pyridinic N were important for current density and onset potential of ORR catalysis, respectively [23]. Nakamura et al. further investigated ORR active sites in N-doped carbon and found that the catalytic activity was created by pyridinic N [24]. By combining experimental data and DFT calculations, Qiao et al. discovered that N and B dual-doped graphene exhibited the lowest overall reaction free energy change [25]. Valentin et al. proved by model simulation that B was highly desirable in forming oxygenated species [26]. B-doped carbon nanotubes were also synthesized by Fan et al. for OER catalysis [27], while the origin of catalytic activity was not fully understood. Generally speaking, the introduction of dopants alters the charge density distribution and the spin density distribution simultaneously, while the change of spin density is more important according to a DFT study [28]. Compared to mono-doped systems, dual-doped systems can generate more significant change in spin density and thus may result in higher catalytic activity [29]. Besides change of spin density, O_2 adsorption is also critical during ORR process. C atoms bonded with more electronegative dopants such as N can serve as O_2 adsorption sites due to a higher density of positive charge, while less electronegative dopants such as B can act as O_2 adsorption sites by themselves [30].

Although many heteroatom-doped carbon materials have been reported, it is still quite challenging to precisely control the even distribution of doped species. For most of the doping approaches such as post-treatment with gas and pyrolysis with precursors [31], there is no guarantee that the doping sites can be distributed evenly in the body of carbon materials, or the doping sites can be easily accessed by reactants. On the other hand, using metal-organic frameworks (MOFs) as precursors to prepare carbon materials may solve the aforementioned problems [32,33]. MOFs are crystalline coordination polymers composed of metal nodes and organic linkers [34]. Because of their special features such as versatile chemical composition, uniform yet tunable pore size, and rich functional group, they have found wide applications in various fields [35–40]. Recently, there have been growing interests in pyrolyzing MOFs as precursors to prepare carbon materials [41,42]. The non-conductive organic moieties in MOFs can be turned into highly conductive carbon matrix after pyrolysis. Meanwhile, heteroatoms such as N and B from MOF precursors can be retained in the pyrolyzed carbon materials with even distribution serving as active sites for ORR and OER catalysis. In addition, by carbothermal reduction and evaporation of low boiling point metals (*e.g.*, Zn) which are adjacent to the heteroatoms, pores and pathways accessible to the active sites may be generated [32]. Surface area of the pyrolyzed products can be further enhanced by adjusting the pyrolysis atmosphere, such as using H_2 and NH_3 [43,44].

Herein, we report the synthesis of a B-N dual-doped highly porous carbon (BNPC) for ORR and OER catalysis by pyrolyzing a Zn-MOF (MC-BIF-1S) under the atmosphere of H_2–Ar mixture. During the process of pyrolysis, Zn was carbothermally reduced and evaporated resulting in metal-free carbon materials, which exhibited high ORR catalytic activity (E_{onset} = 0.894 V vs. RHE), close to 4-electron selectivity (>3.6), and better durability compared to commercial Pt/C catalyst in a 10,000-cycle test. During the OER tests, a current density of 10 mA cm^{-2} at 1.55 V (vs. RHE) in 6 M KOH solution was achieved using BNPCs as the catalyst. In addition, classical two-electrode rechargeable Zn-air batteries were assembled and the air cathodes prepared using BNPCs exhibited comparable performance to some of the most efficient bifunctional metal-free electrocatalysts [22,45]. To the best of our knowledge, this is the first time that MOFs are used to prepare metal-free ORR/OER bifunctional electrocatalysts, which has shed light on the tailored material design for novel electrocatalysts.

2. Experimental section

2.1. Materials and reagents

All the reagents were obtained from commercial suppliers and used without further purification. Sodium tetrakis(1-imidazolyl) borate, 1,4-benzenebicarboxlic acid, imidazole, and $Zn(OAc)_2 \cdot 2H_2O$ were purchased from Sigma Aldrich. 1,3-Dimethyl propyleneurea, 2-propanol, and 5 wt% Nafion solution were purchased from Alfa Aesar.

2.2. Synthesis of MC-BIF-1S

MC-BIF-1S was synthesized according to the previous report [46]. Briefly, sodium tetrakis(1-imidazolyl) borate (0.036 g, 0.12 mmol), 1,4-benzenebicarboxlic acid (0.032 g, 0.19 mmol), imidazole (0.016 g, 0.24 mmol), and $Zn(OAc)_2 \cdot 2H_2O$ (0.043 g, 0.20 mmol) were mixed in 1,3-dimethyl-propyleneurea (2 mL) and the mixture was placed in a 20 mL glass vial, which was kept at 120 °C for 5 days and then cooled to room temperature. MC-BIF-1S was obtained as colourless crystals and washed by ethanol for three times and dried at 80 °C for further usage.

2.3. Synthesis of B-N dual-doped porous carbon (BNPC)

BNPCs were synthesized by pyrolyzing MC-BIF-1S crystals. A ceramic boat containing 300 mg of MC-BIF-1S was placed in a quartz tube, which was sealed and purged with pure Ar for 30 min and then heated under H_2/Ar (5/95) atmosphere at a heating rate of 10 °C min^{-1} to set temperatures and kept for 5 h. For the synthesis of B-N dual-doped carbon (BNC), the pyrolysis atmosphere was changed to pure Ar. The samples obtained after pyrolysis were directly used for material characterization and electrochemical measurements.

2.4. Material characterization

Field-emission scanning electron microscopy (FE-SEM) was conducted on an JEOL JSM-7610F scanning electron microscope (5 kV). Field-emission transmission electron microscopy (FE-TEM) was conducted on a JEOL-TEM 2010F transmission electron microscope (200 kV). Powder X-ray diffraction (PXRD) patterns were obtained on a Bruker D8 Advance X-ray powder diffractometer equipped with a Cu sealed tube (λ = 1.54,178 Å) at a scan rate of 4° min^{-1}. The simulated PXRD pattern was obtained from the reported single-crystal structure of MC-BIF-1S (CCDC #764367) using the program Mercury. Raman spectra were collected on a Horiba Modular Raman system using a 50× objective and a 514.5 nm laser source.

N_2 sorption isotherms were measured up to 1 bar using a Micromeritics ASAP 2020 surface area and pore size analyzer. Before the measurement, the sample (~50 mg) was degassed under reduced pressure (<10^{-2} Pa) at 150 °C for 12 h. UHP grade N_2 and

He were used for all the measurements. The temperature of 77 K was maintained with a liquid nitrogen bath. Pore size distribution data were calculated from the N_2 sorption isotherms based on nonlocal density functional theory (NLDFT) model in the Micromeritics ASAP2020 software package (assuming slit pore geometry).

X-ray photoelectron spectroscopy (XPS) experiments were conducted with a Kratos AXIS Ultra DLD surface analysis instrument using a monochromatic Al Kα radiation (1486.71 eV) at 15 kV as the excitation source. The takeoff angle of the emitted photoelectrons was 90° (the angle between the plane of sample surface and the entrance lens of the detector). Peak position was corrected by referencing the C 1s peak position of adventitious carbon for a sample (284.8 eV), and shifting all other peaks in the spectrum accordingly. Fitting was done using the program CasaXPS. Each relevant spectrum was fit to a Shirley type background to correct for the rising edge of backscattered electrons that shifts the baseline higher at high binding energies. Peaks were fit as asymmetric Gaussian/Lorentzians, with 0–30% Lorentzian character. The FWHM of all sub-peaks was constrained to 0.7–2 eV, as dictated by instrumental parameters, lifetime broadening factors, and broadening due to sample charging. With this native resolution set, peaks were added, and the best fit, using a least-squares fitting routine, was obtained while adhering to the constraints mentioned above.

2.5. Electrochemical measurements

The cyclic voltammetry, ORR activity, 4-electron selectivity, ORR stability, and OER activity of carbon materials were studied using PINE rotating ring-disk electrode (RRDE) with an electrochemical workstation (CH Instruments 760E). The electrolyte was contained in a 5-neck glass cell. A glassy carbon (GC) disk platinum ring RRDE was used as the working electrode (PINE AFE7R9GCPT). The geometric surface area of the GC disk is 0.2475 cm^2. A platinum wire was used as the counter electrode. The reference electrode is an Ag/AgCl electrode filled with 3 M KCl solution. The catalyst ink was made by dispersing 5 mg of catalyst in 1 mL of 0.25 wt% Nafion solution. The ink was sonicated for 1 h and agitated overnight before usage. Before each test, the working electrode was polished with 0.05 μm alumina powder and rinsed with distilled water. Then 20 μL of ink containing about 100 μg of catalyst was pipetted onto the electrode and dried in the air, resulting in a catalyst loading of ca. 0.4 mg cm^{-2}. For electrochemical experiments on 20% Pt/C and RuO_2, catalyst loading was 0.1 mg cm^{-2}. The electrolyte was purged under Ar (or O_2) for at least 30 min before each test and the gas flow was maintained during the experiments.

2.6. Rechargeable Zn-Air battery tests

The air cathode was prepared by dispersing BNPCs in ethanol for 1 h. A 10 wt% of 5 wt% Nafion 117 solution was added afterward and the mixture was further mixed for 1 h. The catalyst slurry was coated on a carbon paper (10 BC, SGL Carbon) and dried at 70 °C for 1 h to achieve a catalyst loading of 2.0 mg cm^{-2} with a working area of 4 cm^2. A zinc plate was used as the anode. The air cathode and the anode were assembled into a plastic cell, which contained 25 mL of aqueous electrolyte (6 M KOH and 0.2 M $ZnCl_2$). Battery cycling tests were carried out using the recurrent galvanic pulse method (Maccor 4300) by discharging and charging at 2 mA cm^{-2} for 300 s. The cycling was lasted for 100 h (600 charge-discharge cycles).

3. Results and discussion

3.1. Synthesis of BNPCs

The successful synthesis of the MOF precursor MC-BIF-1S is confirmed by its PXRD pattern, which matches well with the simulated PXRD pattern from the crystal structure published by Feng et al. (Fig. S1, CCDC #764367) [46]. The organic linkers are bridged by Zn-centered secondary building units (SBUs) including one Zn-O bond and three Zn-N bonds per SBU. Due to its condensed structure, MC-BIF-1S shows barely any porosity from N_2 sorption test (Fig. S2).

The obtained MC-BIF-1S crystals were then pyrolyzed into heteroatom-doped porous carbon materials (Fig. 1). Argon was initially chosen as the pyrolysis atmosphere and the product was named as boron-nitrogen carbon (BNC). Inspired by Quan et al. [43], 5% H_2–Ar mixture gas was also used as pyrolysis atmosphere to enhance the surface area of carbon products. The obtained products from H_2–Ar mixture were named as boron-nitrogen porous carbons (BNPCs). Number after the abbreviation denotes the pyrolysis temperature (°C).

3.2. Characterization of BNPCs

The morphology of MC-BIF-1S and the pyrolyzed products was studied by SEM and TEM. MC-BIF-1S crystals have cubic morphology with well-defined facets that are typical of crystalline MOFs (Fig. 2a). After being pyrolyzed under H_2–Ar mixture atmosphere at high temperatures, the crystals were decomposed into cracked BNPC solids with a porous texture shown in Fig. 2b–d. A recent study on the Fe-N-C materials for ORR catalysis revealed that mass transfer resistance could be largely reduced by sufficient macropores in the catalysts [47]. The cracked and porous texture of BNPC creates many macropores which may serve as channels for the reactants to permeate through the electrode layer, affording enhanced catalytic performance which will be discussed later on. It is worth of noting that the surface morphology of BNC remains more or less the same as that of the MOF precursor (Fig. 2e), confirming the importance of H_2 during pyrolysis in creating cracked and porous textures. We suspect that it is because of the high pyrolysis temperature that H_2 may have a chance to react with the pyrolyzed carbon residues to form gaseous hydrocarbon products resulting in porous textures. In order to justify this hypothesis, we used mass spectrometry (MS) to analyze the possible species in the exhaust gas during pyrolysis. The MS data collected for the exhaust gas at a pyrolysis temperature of 1000 °C under 5% H_2/Ar atmosphere show discernible signals with mass/charge ratio of 16, 28, and 44, which can be attributed to CH_4, C_2H_4, and C_3H_8, respectively (Fig. S3). TEM image of BNPC-1100 (Fig. 2f) reveals the formation of few-layered graphite. The measured lattice spacing is 0.337 nm, which is close to the spacing of (002) plane of graphite (0.335 nm) [48]. Compared with pure graphite, the carbon lattice in BNPC-1100 is highly wrinkled, indicating the doping of heteroatoms [49]. TEM images of BNPC-900, BNPC-1000, and BNC-1000 are also obtained (Fig. S4). Compared to BNPCs, the graphite lattice pattern is harder to be observed in BNC-1000, suggesting the formation of a heteroatom-doped carbon material with lower crystallinity.

The structure of pyrolyzed samples was further studied by PXRD and Raman spectroscopy. The PXRD patterns of all pyrolyzed samples show broad peaks at around 25° [from (002) plane of graphite] and 43° [from (100) plane and (101) plane of graphite], indicating the formation of unordered carbon with low crystallinity (Fig. 3a). However, two additional peaks at around 23 and 36° with increased intensity at higher pyrolysis temperatures show up in the PXRD patterns of BNPCs. These peaks may be attributed to the

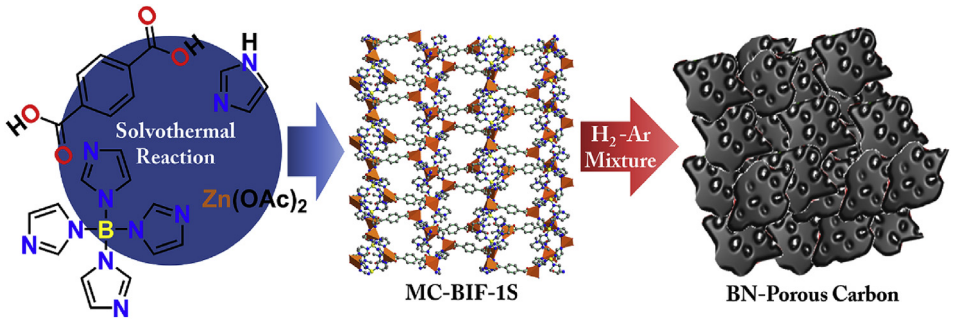

Fig. 1. The synthetic scheme of BNPCs. (A colour version of this figure can be viewed online.)

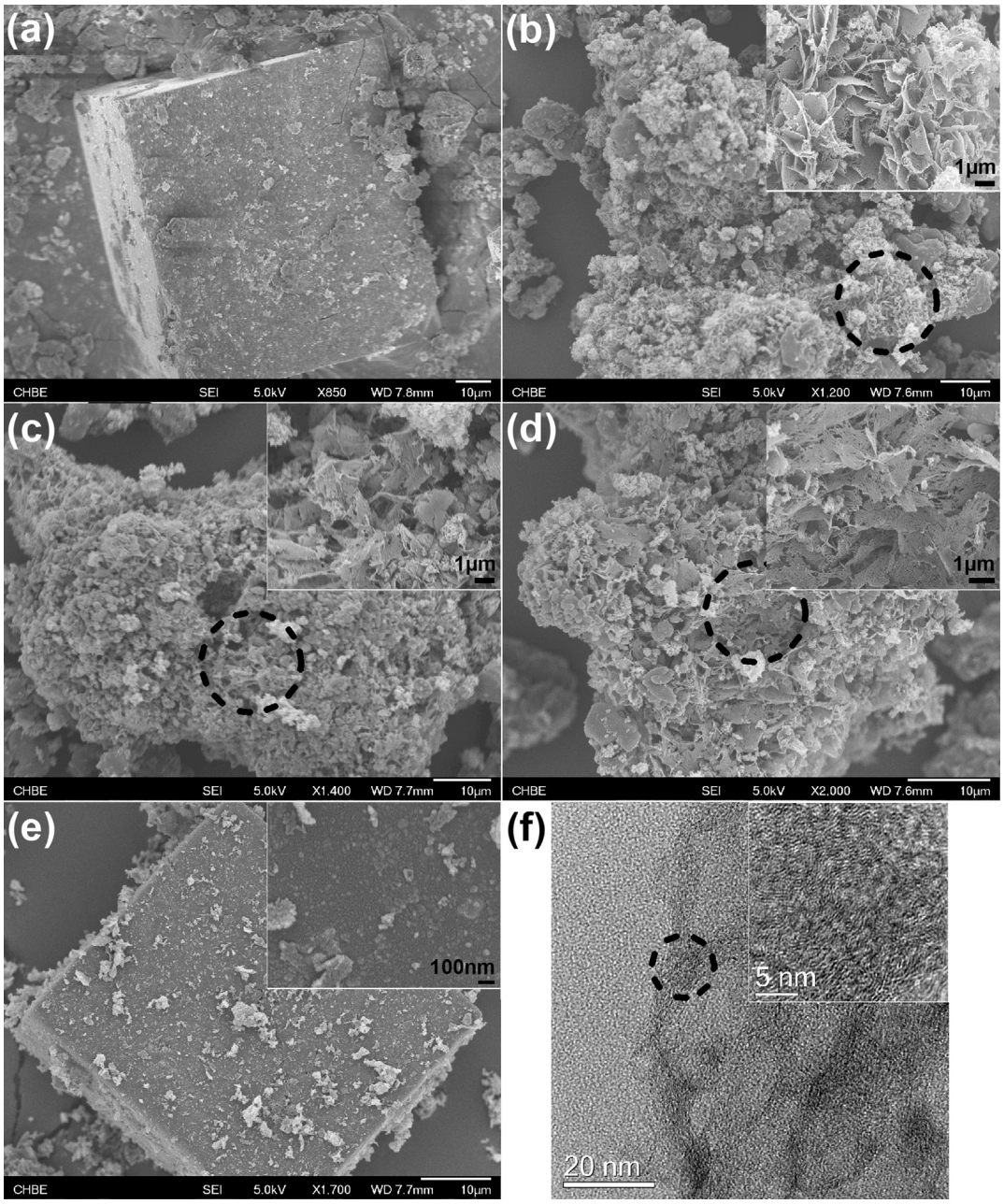

Fig. 2. SEM images of MC-BIF-1S crystal (a), BNPC-900 (b), BNPC-1000 (c), BNPC-1100 (d), and BNC-1000 (e). TEM image of BNPC-1100 (f). Inset areas are marked with cycles.

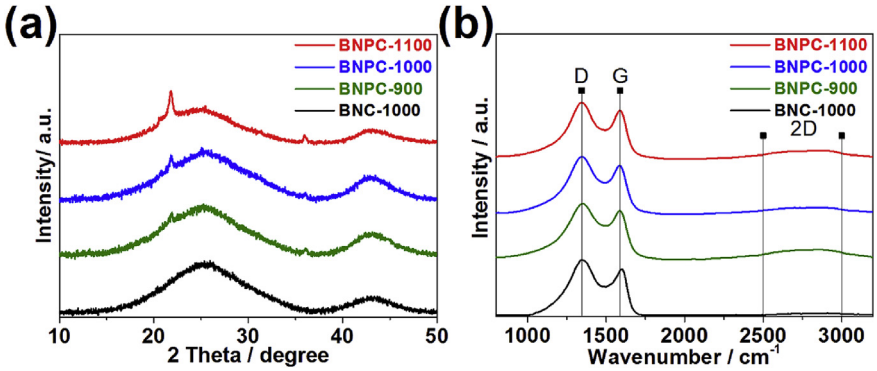

Fig. 3. (a)PXRD patterns and (b) Raman spectra of BNC and BNPCs. (A colour version of this figure can be viewed online.)

ternary C-N-B system, while their exact origin requires further study. Raman spectra of BNC and BNPCs are shown in Fig. 3b. The I_D/I_G is 2.8 for BNC-1000 and 2.2 for BNPCs regardless of the pyrolysis temperature. The difference of I_D/I_G between BNC and BNPCs comes from higher crystallinity of carbon in BNPCs [50]. Broad 2D bands in all samples suggest low order of carbon, which is common in carbon materials obtained by pyrolysis [51].

The successful heteroatom doping and the chemical states of dopants were investigated by XPS (Fig. 4a and b). The co-existence of B and N is confirmed by their characteristic 1s photoelectron peaks. The N 1s XPS spectra can be deconvoluted into three peaks with binding energy of ca. 398.3, 399.2, and 400.4 eV, representing pyridinic N with N-B-C moiety, pyrrolic N, and quaternary N, respectively [52,53]. Due to the slight difference in binding energy, the signals from pyridinic N and N-B-C moiety are indistinguishable from the XPS spectra. Among BNPCs, the content of pyrrolic N decreases with increased pyrolysis temperature due to its relatively low stability [54], while the content of pyridinic N with N-B-C moiety keeps increasing with increased pyrolysis temperature until 74.64% at 1100 °C. The percentage of quaternary N shows little dependence on pyrolysis temperature (13.16, 21.88, and 12.46% at 900, 1000, and 1100 °C, respectively). For BNC-1000, pyrrolic N accounts for about 70% of all N species, which is much higher than that in all BNPCs. The B 1s XPS spectra of BNC and BNPCs are shown in Fig. 3b. Unlike N, B species in BNPCs are less affected by pyrolysis temperature. Signals from B in N-B-C moieties (~30%) and BC_2O (~70%) are dominant in all BNPCs, while the signal of BC_2O disappears and BCO_2 is presented in BNC-1000 [53]. It is obvious that pyrolysis in the presence of H_2 has notable effect on the chemical states of the dopants. In addition, EDS elemental mapping was performed on BNPC-1100 to show the uniform distribution of doped B and N elements (Fig. S5). There is no signal of Zn 2p in either full XPS spectra (Fig. S6) or high resolution scans (Fig. S7), indicating that Zn has been completely removed during high temperature pyrolysis under the mechanism of carbothermal reduction and evaporation [55].

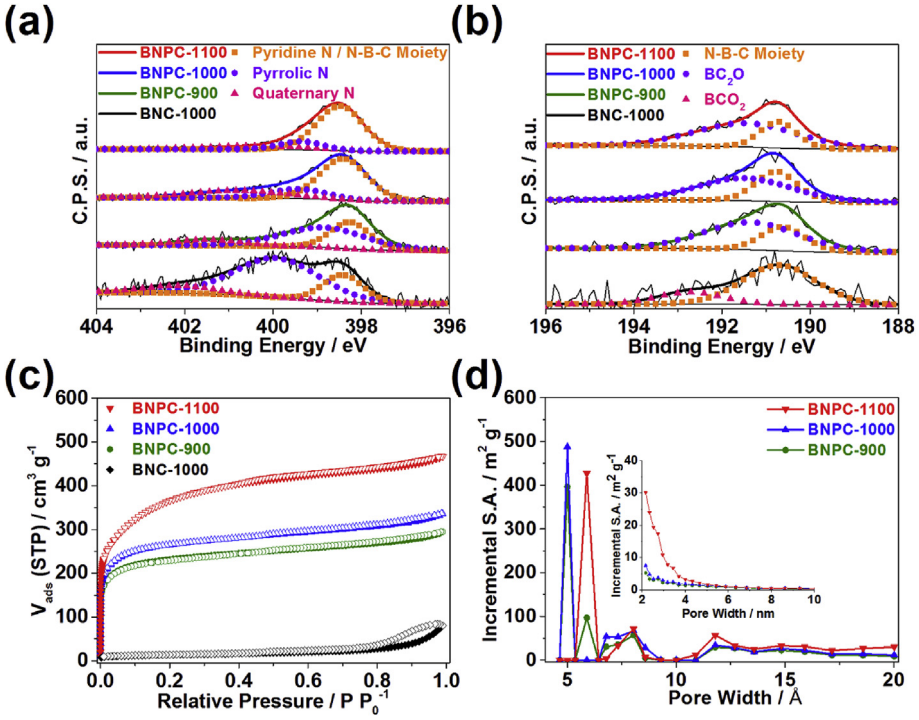

Fig. 4. (a) N 1*s* and (b) B 1*s* high resolution XPS spectra; (c) N_2 sorption isotherms and (d) pore size distribution of BNC and BNPCs. (A colour version of this figure can be viewed online.)

Elemental analyses were performed to quantify the chemical composition of pyrolyzed products (Table S1). Among all the pyrolyzed samples, the C content stays at around 70 wt% regardless of the pyrolysis temperature. The N content is around 9 wt% for BNC-1000, BNPC-900, and BNPC-1000, but drops to 7.29 wt% for BNPC-1100 suggesting that higher pyrolysis temperature is unfavorable for N retention [56]. B content in BNPCs (~5 wt%) is higher than that in BNC-1000 (3.18 wt%), possibly due to the loss of O-containing species by pyrolyzing in H_2-containg atmosphere leading to a relative increase in the content of other elements. Trace amount of Zn can be detected in BNC-1000 but is completely missing in BNPCs suggesting the complete removal of Zn by pyrolysis under H_2-containg atmosphere.

Surface area and pore size distribution of the pyrolyzed samples were studied by N_2 sorption at 77 K (Fig. 4c and d). The BNC sample shows a negligible surface area, suggesting an unsuccessful pore formation from the non-porous MC-BIF-1S precursor only by Zn evaporation through pyrolysis in pure Ar atmosphere. On the contrary, the surface area of BNPCs being pyrolyzed in H_2-containing atmosphere increases by about 20-fold, especially at higher pyrolysis temperatures (Table 1). The additional H_2 may serve as a surface area enhancer during pyrolysis in the following two ways. It can react with the carbon residue yielding gases products as evidenced by the previous MS result, resulting in more cracks and porous textures similar to the effect of introducing CO_2 and NH_3 in the production of activated carbon [57,58]. In addition, it may facilitate the process of carbothermal reduction and evaporation of Zn, which is proven by the lower Zn content in BNPCs than that in BNC (Table S1).

All N_2 sorption isotherms of BNPCs exhibit Type I shape with slight hystereses, suggesting mainly microporous structures (pore size less than 2 nm) with a small portion of mesopores (pore size between 2 and 50 nm). The major pores (>60%) are in microporous range (5 Å, Table 1). However, BNPC-1100 has larger micropores (6 Å) and more pores belonging to mesopores, which can be attributed to the higher vapor pressure of Zn and other small molecules at higher pyrolysis temperature facilitating the pore-forming process. Being rich in micropores may expose more catalytic active sites, while mesopores are beneficial to the mass transfer process. Therefore, it is anticipated that BNPC-1100 will demonstrate better catalytic activity and kinetics, which has been proven in other catalysts with hierarchical porosity [59].

3.3. Electrochemical measurements

The electrochemical properties of BNPCs were investigated by an electrochemical workstation combined with a rotating ring-disk electrode (RRDE) system. The cyclic voltammetry (CV) curves of BNPC-1100 and 20% Pt/C in Ar and O_2-saturated 0.1 M KOH are shown in Fig. 5a. The rectangular shape of BNPC-1100 CV curve in Ar suggests a pure capacitive behavior under inert atmosphere. The peak at ~0.7 V (vs. RHE) in O_2-saturated electrolyte indicates ORR catalytic activity of BNPC. CV curves of the rest samples are shown in Fig. S8 and they all demonstrate similar behavior.

Cathodic linear sweep voltammetry (CLSV) curves obtained at 1600 rpm in O_2-saturated 0.1 M KOH for BNC, BNPCs, and two pyrolyzed MOF and COF (ZIF-8 and COF-5) [60,61] without co-doping were used to study the effects of pyrolysis atmosphere, pyrolysis temperature, and B-N-co-doping on ORR catalytic activity (Fig. 5b, Table 1). The catalysts obtained by pyrolyzing in H_2—Ar mixed atmosphere (BNPCs) all demonstrate better catalytic activity than the one obtained by pyrolyzing in pure Ar (BNC), which can be attributed to the higher porosity and larger pyridinic N content in BNPCs. Higher porosity helps the mass transfer of the heterogeneous catalytic process of ORR, while pyridinic N has recently been found to be the major active sites for ORR catalysis [24]. Pyrolysis temperature is also an important parameter in affecting the ORR catalytic activity. BNPC-900 shows the highest limiting current (4.92 mA cm^{-2}) while BNPC-1000 is more active at lower potential range (<0.6 V vs. RHE). Among the three, BNPC-1100 has the highest onset potential (0.894 V vs. RHE) and the best kinetics ($E_{half\ wave}$ = 0.803 V) due to its high surface area and large content of pyridinic N. ZIF-8 and COF-5, two common MOF and COF containing either N or B, were pyrolyzed as well to examine the effect of B-N co-doping on ORR catalysis (Figs. S9 and S10). Because of its ultra-high surface area and easily accessible active sites, pyrolyzed ZIF-8 shows high onset potentials. However, the activity of the active sites is relatively low, leading to low current densities at E < 0.8 V and a poor overall ORR catalytic performance. The pyrolyzed COF-5 has slightly higher current densities at E < 0.8 V, but with lower onset potentials possibly due to its lower surface area and partially inaccessible active sites (Table 1). Compared with them, BNPC-1100 exhibits balanced high onset potentials and current densities, demonstrating the high catalytic activity caused by co-doping. Kinetic current densities at 0.7 V of the tested samples are shown in Fig. 5c. BNPC-1100 has the highest J_k of 7.60 mA cm^{-2}, which is comparable to some of the best graphene oxide derived and metal-containing ORR electrocatalysts [62,63].

Two different methods were used to find out the pathway of ORR catalyzed by BNPCs. Electron transfer number and peroxide yield can be directly obtained by RRDE measurements (Fig. 5d and S11). Among BNPCs, BNPC-1100 shows the highest number of

Table 1
A summary of surface area, micropore-mesopore ratio, ORR and OER catalytic performance of pyrolyzed ZIF-8, pyrolyzed ZIF-11, BNC, BNPCs, 20% Pt/C, and RuO_2.

	Surface area and pore size distribution			ORR catalytic activity[c]			OER catalytic activity[c]	
	BET SA[a] and V_{TotalP}[b]	Micropore SA[a] and V_{MicroP}[b]	Mesopore SA[a] and V_{MesoP}[b]	E_{onset}[d] (V)	$E_{half\ wave}$[e] (V)	j_{max}[f] (mA cm^{-2})	E_{onset} (V)	j @ 1.6 V[g] (mA cm^{-2})
Pyrolyzed ZIF-8	1409, 0.71	1215, 0.47	39, 0.05	0.901	0.786	3.29	1.74	/
Pyrolyzed COF-5	561, 0.37	212, 0.16	14, 0.03	0.871	0.780	3.87	1.58	0.18
BNC-1000	48	/	/	0.857	0.746	3.68	N.D.	0.37
BNPC-900	885, 0.36	766, 0.28	28, 0.04	0.861	0.769	4.92	1.48	1.69
BNPC-1000	1010, 0.42	859, 0.32	35, 0.05	0.862	0.749	4.69	1.41	3.64
BNPC-1100	1348, 0.59	809, 0.37	130, 0.17	0.894	0.793	4.73	1.38	4.94
20% Pt/C	/	/	/	0.946	0.803	5.26	1.69	/
RuO_2	/	/	/	/	/	/	1.45	1.50

[a] $m^2\ g^{-1}$.
[b] $cm^3\ g^{-1}$.
[c] In 0.1 M KOH.
[d] Determined as j = 0.1 mA cm^{-2}.
[e] The point having the largest slope in the mixed-control zone.
[f] At 0.2 V versus RHE.
[g] Versus RHE; N.D. Not determined.

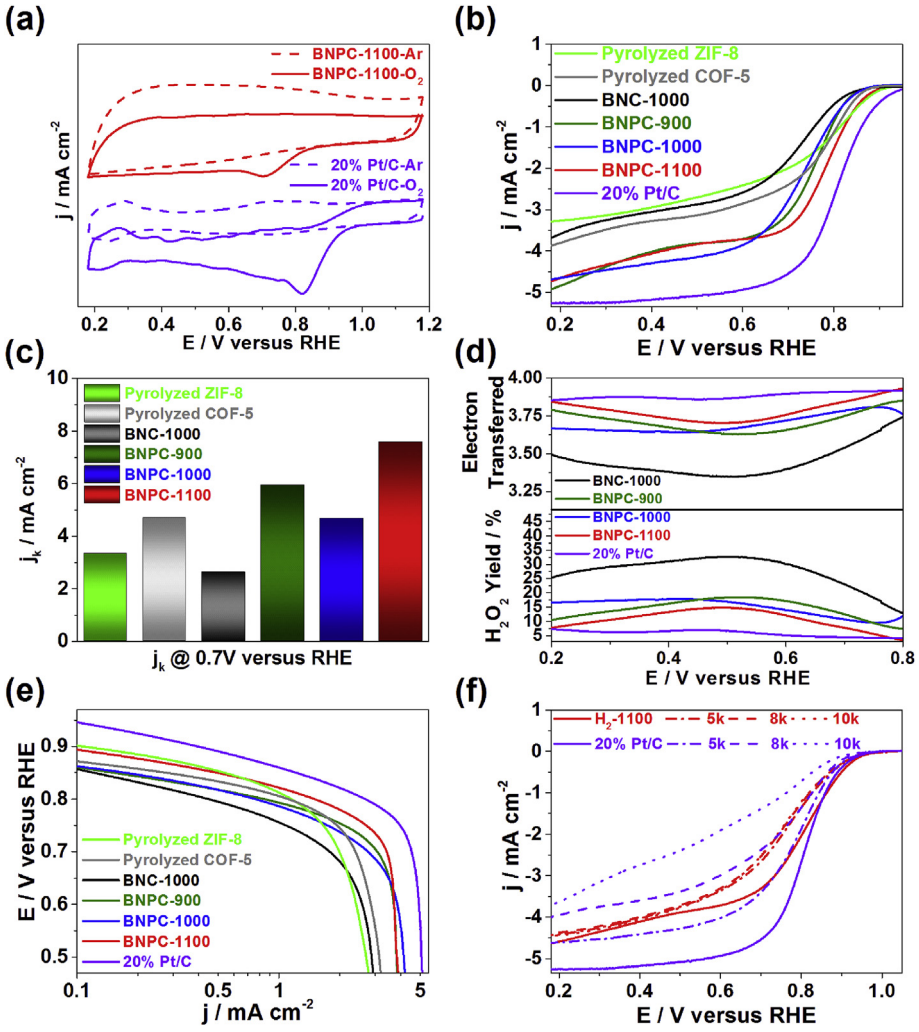

Fig. 5. (a) CVs of BNPC-1100 and 20% Pt/C in 0.1 M KOH; (b) CLSVs of BNC, BNPCs and non-B-doped carbon at 1600 rpm; (c) Kinetic current densities of tested metal-free ORR catalysts at 0.7 V vs. RHE; (d) Number of electrons transferred and H_2O_2 yields of BNC, BNPCs and 20% Pt/C determined by RRDE measurements; (e) Tafel plots of 20% Pt/C, BNC and BNPCs measured in O_2-saturated 0.1 M KOH aqueous solution at 1600 rpm; (f) ORR catalytic performance of BNPC-1100 and 20% Pt/C before and after 5000, 8000 and 10,000 accelerated degradation test cycles. (A colour version of this figure can be viewed online.)

electron transferred (>3.7 in the potential range of 0.8–0.2 V vs. RHE) and the lowest peroxide yield (<15%). Alternatively, by varying the rotation speed, CLSVs at different rotation speeds were obtained (Fig. S12) and Koutecky–Levich (K–L) plots were derived (Fig. S13). The K-L plots show good linearity and the calculated number of electron transferred of BNPC-1100 is over 3.6, indicating a highly efficient ORR catalytic process. Results calculated by K-L equations are consistent with that obtained by RRDE tests, proving that ORR catalyzed by BNPCs is mainly via an efficient 4-electron pathway. Tafel plots derived from CLSV curves are shown in Fig. 5e. The carbon-based catalysts and 20% Pt/C all exhibit a similar slope of ca. 80 mV dec^{-1}, indicating that these catalysts share the same rate determining step: the protonation of O_2^- [64].

Stability is critical to all catalysts during their applications. In order to test the stability, accelerated degradation tests (ADT) were performed on BNPC-1100 as well as the commercial 20% Pt/C catalyst as a reference. Fig. 5f shows the ORR catalytic performance of BNPC-1100 and 20% Pt/C before and after 5000, 8000, and 10,000 ADT cycles. Although both of their current densities decrease after several ADT cycles, it is interesting to note that the ORR catalytic performance of BNPC-1100 stabilizes after 5000 cycles while there is a continuous loss of catalytic activity in 20% Pt/C during further ADT cycles, resulting in even worse activity than BNPC-1100 after 8000 ADT cycles. The continuous deteriorated ORR activity of 20% Pt/C can be attributed to the gradual loss of electrochemical active surface area of Pt/C under the ADT condition [65], which can be largely avoided in the metal-free BNPC-1100. The above ADT results prove that our metal-free ORR catalyst has better stability than commercial Pt/C, which is extremely helpful in long-term usage [66].

The OER during charging process of rechargeable Zn-air batteries is equally important for their operation. The OER catalytic activity of BNC and BNPCs is measured along with 20% Pt/C and RuO_2, one of the benchmark noble metal oxide OER catalysts, as references. From the anodic linear sweep voltammetry (ALSV) curves in 0.1 M KOH (Fig. 6a), it is clear that BNPCs show much better OER activity than BNC, non-co-doped carbons, and 20% Pt/C (Table 1). Compared to RuO_2, BNPC-1100 has a smaller onset potential of OER, indicating the presence of highly OER active sites. The second lowest slope in the semi-log plot revealed by the Tafel plot also suggests its high OER efficiency (Fig. 6c). In fact, BNPC-1100 has comparable or even better OER catalytic performance compared to some of the top non-metal OER catalysts reported so far (Table S2). However, its stability at higher potentials (>1.8 V in 0.1 M KOH)

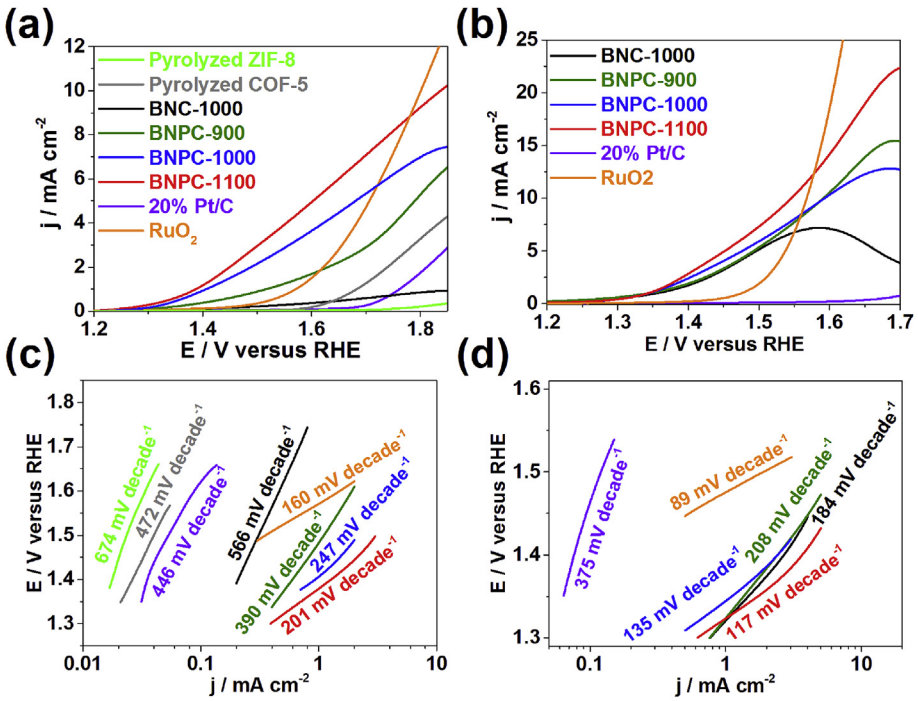

Fig. 6. ALSVs and Tafel plots of pyrolyzed non-B doped MOFs, BNC, BNPCs, 20% Pt/C and RuO_2 in 0.1 M KOH (a, c) and 6 M KOH (b, d). (A colour version of this figure can be viewed online.)

remains to be further improved. Chronopotentiometry was performed to investigate its stability at lower potentials, and it was found that BNPC-1100 was able for at least 10 h without significant degradation (Fig. S14). After switching the electrolyte to 6 M KOH which is commonly used in rechargeable Zn-air batteries, the reaction currents dramatically increase (Fig. 6b). Still, BNPC-1100 exhibits the highest OER catalytic current among all the carbon-based catalysts in this study and the second lowest slope in the Tafel plots (Fig. 6d). Considering the previous results, the excellent OER catalytic activity of BNPC-1100 may come from its higher porosity and B-N dual-doped chemical structure. It is known that the adsorption of OH^- and H_2O is critical to initiate the OER process, and the positively charged C atoms around the N dopants as well as the B dopants provide sufficient sites to promote the electron transfer between catalyst and reactants [67]. Further studies, both experimental and theoretical, are needed to unveil the OER catalytic mechanism of B-N dual-doped carbon materials.

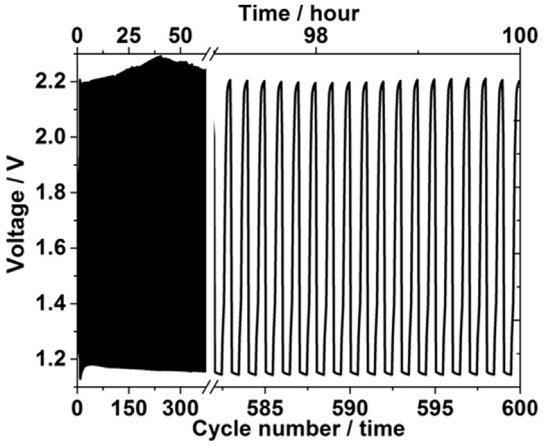

Fig. 7. Cycling performance of the rechargeable Zn-air battery using BNPC-1100 as the air cathode. A cycle consists of a discharging stage and a charging stage for 300 s respectively at 2 mA cm^{-2}.

3.4. Rechargeable Zn-air battery tests

The above results have strongly indicated the potential of BNPC-1100 to be used as an ORR/OER bifunctional electrocatalyst in rechargeable Zn-air batteries. In order to prove this, a classic two-electrode rechargeable Zn-air battery was assembled and BNPC-1100 was used as the catalyst loaded onto the air cathode. The cycling performance of the assembled battery is shown in Fig. 7. Encouragingly, the battery was tested for a continuous period of 100 h without significant performance loss at a charge-discharge current density of 2 mA cm^{-2}. Although the cathodic material underwent an activation process and the charging voltage increased to around 2.3 V at the early stage of the test, it gradually reduced and the final voltages for discharge and charge after 100 h of test were almost the same as the initial values (2.19 V for charge and 1.16 V for discharge). Polarization potential on the electrodes was determined to make sure that the carbonaceous catalyst was not oxidized during the charging process (Fig. S15). In comparison, BNPC-1000 was also evaluated in a single battery test and the result is shown in Fig. S16. The discharging voltage is lower (1.12 V) and it shows a deteriorating trend during the 100-h cycling test (Fig. S17). This suggests that BNPC-1100 has a high retention of ORR/OER catalytic activity under an actual working condition of rechargeable Zn-air batteries. The discharging voltage and the columbic efficiency of our system are 1.14 V and 52%, respectively, which are comparable or even better than the top metal-free air cathodes for Zn-air batteries reported so far [22,45]. Our results have clearly demonstrated the huge potential of MOF-derived metal-free ORR/OER bifunctional electrocatalysts in rechargeable Zn-air batteries.

4. Conclusion

In summary, we have synthesized highly porous, B-N dual-doped carbon materials by pyrolyzing a MOF precursor under H_2-containing atmosphere. The high porosity and introduction of N and B in these carbon materials can effectively improve their ORR catalytic performance. Meanwhile, high OER catalytic activity of these materials has also been proven at low potentials. Of all the carbon materials, the one pyrolyzed at 1100 °C (BNPC-1100) shows the best performance due to the combined features of high porosity, B-N dual-doping, and high pyridinic N content. In addition, BNPC-1100 exhibits comparable or even better catalytic performance to those top bifunctional metal-free catalysts when being fabricated into air cathodes of rechargeable Zn-air batteries and tested under working conditions. We have demonstrated for the first time that MOFs can be used as precursors to synthesize metal-free ORR/OER bifunctional cathodic electrocatalysts with great potential in rechargeable Zn-air batteries.

Acknowledgements

This work is supported by National University of Singapore (CENGas R-261-508-001-646) and Singapore Ministry of Education (MOE AcRF Tier 1 R-279-000-410-112, AcRF Tier 2 R-279-000-429-112).

Appendix A. Supplementary data

Supplementary data related to this article can be found at http://dx.doi.org/10.1016/j.carbon.2016.10.046.

References

[1] A. Vlad, N. Singh, C. Galande, P.M. Ajayan, Design considerations for unconventional electrochemical energy storage architectures, Adv. Energy Mater. 5 (2015) 201402115.
[2] R. Cao, J.-S. Lee, M. Liu, J. Cho, Recent progress in non-precious catalysts for metal-air batteries, Adv. Energy Mater. 2 (7) (2012) 816–829.
[3] Y. Li, H. Dai, Recent advances in zinc-air batteries, Chem. Soc. Rev. 43 (15) (2014) 5257–5275.
[4] E. Sayilgan, T. Kukrer, F. Ferella, A. Akcil, F. Veglio, M. Kitis, Reductive leaching of manganese and zinc from spent alkaline and zinc–carbon batteries in acidic media, Hydrometallurgy 97 (1) (2009) 73–79.
[5] F. Cheng, J. Chen, Metal-air batteries: from oxygen reduction electrochemistry to cathode catalysts, Chem. Soc. Rev. 41 (6) (2012) 2172–2192.
[6] C. Song, J. Zhang, Electrocatalytic Oxygen Reduction Reaction, PEM Fuel Cell Electrocatalysts and Catalyst Layers, Springer, 2008, pp. 89–134.
[7] Y. Lee, J. Suntivich, K.J. May, E.E. Perry, Y. Shao-Horn, Synthesis and activities of rutile IrO2 and RuO2 nanoparticles for oxygen evolution in acid and alkaline solutions, J. Phys. Chem. Lett. 3 (3) (2012) 399–404.
[8] M.E.G. Lyons, L.D. Burke, Mechanism of oxygen reactions at porous oxide electrodes. Part 1.-Oxygen evolution at RuO2 and RuSn1-O2 electrodes in alkaline solution under vigorous electrolysis conditions, J. Chem. Soc. Faraday Trans. 1 Phys. Chem. Condens. Phases 83 (2) (1987) 299–321.
[9] L. Jörissen, Bifunctional oxygen/air electrodes, J. Power Sources 155 (1) (2006) 23–32.
[10] Y. Wang, T. Zhou, K. Jiang, P. Da, Z. Peng, J. Tang, B. Kong, W.-B. Cai, Z. Yang, G. Zheng, Reduced mesoporous Co3O4 nanowires as efficient water oxidation electrocatalysts and supercapacitor electrodes, Adv. Energy Mater 4 (2014) 201400696.
[11] X. Fan, Z. Peng, R. Ye, H. Zhou, X. Guo, M3C (M: Fe, Co, Ni) nanocrystals encased in graphene nanoribbons: an active and stable bifunctional electrocatalyst for oxygen reduction and hydrogen evolution reactions, ACS Nano 9 (7) (2015) 7407–7418.
[12] D. Deng, L. Yu, X. Chen, G. Wang, L. Jin, X. Pan, J. Deng, G. Sun, X. Bao, Iron encapsulated within pod-like carbon nanotubes for oxygen reduction reaction, Angew. Chem. Int. Ed. 52 (1) (2013) 371–375.
[13] G. Zhang, B.Y. Xia, C. Xiao, L. Yu, X. Wang, Y. Xie, X.W. Lou, General formation of complex tubular nanostructures of metal oxides for the oxygen reduction reaction and lithium-ion batteries, Angew. Chem. Int. Ed. 52 (33) (2013) 8643–8647.
[14] T.Y. Ma, S. Dai, M. Jaroniec, S.Z. Qiao, Metal–organic framework derived hybrid Co3O4-carbon porous nanowire arrays as reversible oxygen evolution electrodes, J. Am. Chem. Soc. 136 (39) (2014) 13925–13931.
[15] J. Zhao, K. Jarvis, P. Ferreira, A. Manthiram, Performance and stability of Pd–Pt–Ni nanoalloy electrocatalysts in proton exchange membrane fuel cells, J. Power Sources 196 (10) (2011) 4515–4523.
[16] S. Chen, J. Duan, M. Jaroniec, S.Z. Qiao, Nitrogen and oxygen dual-doped carbon hydrogel film as a substrate-free electrode for highly efficient oxygen evolution reaction, Adv. Mater. 26 (18) (2014) 2925–2930.
[17] T.Y. Ma, S. Dai, M. Jaroniec, S.Z. Qiao, Graphitic carbon nitride nanosheet–carbon nanotube three-dimensional porous composites as high-performance oxygen evolution electrocatalysts, Angew. Chem. Int. Ed. 53 (28) (2014) 7281–7285.
[18] K. Gong, F. Du, Z. Xia, M. Durstock, L. Dai, Nitrogen-doped carbon nanotube arrays with high electrocatalytic activity for oxygen reduction, Science 323 (5915) (2009) 760–764.
[19] S. Yang, L. Zhi, K. Tang, X. Feng, J. Maier, K. Müllen, Efficient synthesis of heteroatom (N or S)-doped graphene based on ultrathin graphene oxide-porous silica sheets for oxygen reduction reactions, Adv. Funct. Mater. 22 (17) (2012) 3634–3640.
[20] C. Zhang, N. Mahmood, H. Yin, F. Liu, Y. Hou, Synthesis of phosphorus-doped graphene and its multifunctional applications for oxygen reduction reaction and lithium ion batteries, Adv. Mater. 25 (35) (2013) 4932–4937.
[21] T.V. Vineesh, M.P. Kumar, C. Takahashi, G. Kalita, S. Alwarappan, D.K. Pattanayak, T.N. Narayanan, Bifunctional electrocatalytic activity of boron-doped graphene derived from boron carbide, Adv. Energy Mater. (2015) 1500658.
[22] J. Zhang, Z. Zhao, Z. Xia, L. Dai, A metal-free bifunctional electrocatalyst for oxygen reduction and oxygen evolution reactions, Nat. Nano 10 (5) (2015) 444–452.
[23] L. Lai, J.R. Potts, D. Zhan, L. Wang, C.K. Poh, C. Tang, H. Gong, Z. Shen, J. Lin, R.S. Ruoff, Exploration of the active center structure of nitrogen-doped graphene-based catalysts for oxygen reduction reaction, Energy Environ. Sci. 5 (7) (2012) 7936–7942.
[24] D. Guo, R. Shibuya, C. Akiba, S. Saji, T. Kondo, J. Nakamura, Active sites of nitrogen-doped carbon materials for oxygen reduction reaction clarified using model catalysts, Science 351 (6271) (2016) 361–365.
[25] Y. Jiao, Y. Zheng, M. Jaroniec, S.Z. Qiao, Origin of the electrocatalytic oxygen reduction activity of graphene-based catalysts: a roadmap to achieve the best performance, J. Am. Chem. Soc. 136 (11) (2014) 4394–4403.
[26] L. Ferrighi, M. Datteo, C. Di Valentin, Boosting graphene reactivity with oxygen by boron doping: density functional theory modeling of the reaction path, J. Phys. Chem. C 118 (1) (2013) 223–230.
[27] Y. Cheng, Y. Tian, X. Fan, J. Liu, C. Yan, Boron doped multi-walled carbon nanotubes as catalysts for oxygen reduction reaction and oxygen evolution reactionin in alkaline media, Electrochim. Acta 143 (2014) 291–296.
[28] L. Zhang, Z. Xia, Mechanisms of oxygen reduction reaction on nitrogen-doped graphene for fuel cells, J. Phys. Chem. C 115 (22) (2011) 11170–11176.
[29] J. Liang, Y. Jiao, M. Jaroniec, S.Z. Qiao, Sulfur and nitrogen dual-doped mesoporous graphene electrocatalyst for oxygen reduction with synergistically enhanced performance, Angew. Chem. Int. Ed. 51 (46) (2012) 11496–11500.
[30] L. Yang, S. Jiang, Y. Zhao, L. Zhu, S. Chen, X. Wang, Q. Wu, J. Ma, Y. Ma, Z. Hu, Boron-Doped carbon nanotubes as metal-free electrocatalysts for the oxygen reduction reaction, Angew. Chem. 123 (31) (2011) 7270–7273.
[31] J.P. Paraknowitsch, A. Thomas, Doping carbons beyond nitrogen: an overview of advanced heteroatom doped carbons with boron, sulphur and phosphorus for energy applications, Energy Environ. Sci. 6 (10) (2013) 2839–2855.
[32] Q. Xu, Z. Guo, M. Zhang, Z. Hu, Y. Qian, D. Zhao, Highly efficient photocatalysts by pyrolyzing a Zn-Ti heterometallic metal-organic framework, CrystEngComm 18 (2016) 4046–4052.
[33] Z. Guo, J.K. Cheng, Z. Hu, M. Zhang, Q. Xu, Z. Kang, D. Zhao, Metal-organic frameworks (MOFs) as precursors towards TiO x/C composites for photodegradation of organic dye, RSC Adv. 4 (65) (2014) 34221–34225.
[34] S. Kitagawa, Metal–organic frameworks (MOFs), Chem. Soc. Rev. 43 (16) (2014) 5415–5418.
[35] D. Zhao, D. Yuan, H.-C. Zhou, The current status of hydrogen storage in metal–organic frameworks, Energy Environ. Sci. 1 (2) (2008) 222–235.
[36] T. Rodenas, M. van Dalen, E. García-Pérez, P. Serra-Crespo, B. Zornoza, F. Kapteijn, J. Gascon, Visualizing MOF mixed matrix membranes at the nanoscale: towards structure-performance relationships in CO2/CH4 separation over NH2-MIL-53 (Al)@ PI, Adv. Funct. Mater. 24 (2) (2014) 249–256.
[37] Z.Y. Gu, J. Park, A. Raiff, Z. Wei, H.C. Zhou, Metal–organic frameworks as biomimetic catalysts, ChemCatChem 6 (1) (2014) 67–75.
[38] M. Zhang, G. Feng, Z. Song, Y.-P. Zhou, H.-Y. Chao, D. Yuan, T.T. Tan, Z. Guo, Z. Hu, B.Z. Tang, Two-dimensional metal–organic framework with wide channels and responsive turn-on fluorescence for the chemical sensing of volatile organic compounds, J. Am. Chem. Soc. 136 (20) (2014) 7241–7244.
[39] A.S. Hall, A. Kondo, K. Maeda, T.E. Mallouk, Microporous brookite-phase titania made by replication of a metal–organic framework, J. Am. Chem. Soc. 135 (44) (2013) 16276–16279.
[40] L. Zhang, H.B. Wu, R. Xu, X.W. Lou, Porous Fe2O3 nanocubes derived from MOFs for highly reversible lithium storage, CrystEngComm 15 (45) (2013) 9332–9335.
[41] L. Lux, K. Williams, S. Ma, Heat-treatment of metal–organic frameworks for green energy applications, CrystEngComm 17 (1) (2015) 10–22.
[42] W. Xia, A. Mahmood, R. Zou, Q. Xu, Metal-organic frameworks and their derived nanostructures for electrochemical energy storage and conversion, Energy Environ. Sci. 8 (7) (2015) 1837–1866.
[43] Y. Liu, X. Quan, X. Fan, H. Wang, S. Chen, High-yield electrosynthesis of

hydrogen peroxide from oxygen reduction by hierarchically porous carbon, Angew. Chem. Int. Ed. 54 (23) (2015) 6837–6841.
[44] X. Wang, C.-G. Liu, D. Neff, P.F. Fulvio, R.T. Mayes, A. Zhamu, Q. Fang, G. Chen, H.M. Meyer, B.Z. Jang, S. Dai, Nitrogen-enriched ordered mesoporous carbons through direct pyrolysis in ammonia with enhanced capacitive performance, J. Mater. Chem. A 1 (27) (2013) 7920–7926.
[45] Z. Chen, A. Yu, D. Higgins, H. Li, H. Wang, Z. Chen, Highly active and durable core–corona structured bifunctional catalyst for rechargeable metal–air battery application, Nano Lett. 12 (4) (2012) 1946–1952.
[46] S. Zheng, T. Wu, J. Zhang, M. Chow, R.A. Nieto, P. Feng, X. Bu, Porous metal carboxylate boron imidazolate frameworks, Angew. Chem. Int. Ed. 49 (31) (2010) 5362–5366.
[47] J. Shui, C. Chen, L. Grabstanowicz, D. Zhao, D.-J. Liu, Highly efficient nonprecious metal catalyst prepared with metal–organic framework in a continuous carbon nanofibrous network, Proc. Natl. Acad. Sci. 112 (34) (2015) 10629–10634.
[48] S. Helveg, C. Lopez-Cartes, J. Sehested, P.L. Hansen, B.S. Clausen, J.R. Rostrup-Nielsen, F. Abild-Pedersen, J.K. Norskov, Atomic-scale imaging of carbon nanofibre growth, Nature 427 (6973) (2004) 426–429.
[49] C.H. Choi, M.W. Chung, S.H. Park, S.I. Woo, Additional doping of phosphorus and/or sulfur into nitrogen-doped carbon for efficient oxygen reduction reaction in acidic media, PCCP 15 (6) (2013) 1802–1805.
[50] C. Li, D. Li, J. Yang, X. Zeng, W. Yuan, Preparation of single- and few-layer graphene sheets using Co deposition on SiC substrate, J. Nanomater. 2011 (2011) 7.
[51] L. Wang, C. Schutz, G. Salazar-Alvarez, M.-M. Titirici, Carbon aerogels from bacterial nanocellulose as anodes for lithium ion batteries, RSC Adv. 4 (34) (2014) 17549–17554.
[52] H. Wang, T. Maiyalagan, X. Wang, Review on recent progress in nitrogen-doped graphene: synthesis, characterization, and its potential applications, ACS Catal. 2 (5) (2012) 781–794.
[53] Y. Zhao, L. Yang, S. Chen, X. Wang, Y. Ma, Q. Wu, Y. Jiang, W. Qian, Z. Hu, Can boron and nitrogen co-doping improve oxygen reduction reaction activity of carbon nanotubes? J. Am. Chem. Soc. 135 (4) (2013) 1201–1204.
[54] T. Sharifi, G. Hu, X. Jia, T. Wågberg, Formation of active sites for oxygen reduction reactions by transformation of nitrogen functionalities in nitrogen-doped carbon nanotubes, ACS Nano 6 (10) (2012) 8904–8912.
[55] H.-L. Jiang, B. Liu, Y.-Q. Lan, K. Kuratani, T. Akita, H. Shioyama, F. Zong, Q. Xu, From metal–organic framework to nanoporous carbon: toward a very high surface area and hydrogen uptake, J. Am. Chem. Soc. 133 (31) (2011) 11854–11857.
[56] W. Zhang, Y. Liu, G. Lu, Y. Wang, S. Li, C. Cui, J. Wu, Z. Xu, D. Tian, W. Huang, J.S. DuCheneu, W.D. Wei, H. Chen, Y. Yang, F. Huo, Mesoporous metal-organic frameworks with size-, shape-, and space-distribution-controlled pore structure, Adv. Mater. 27 (18) (2015) 2923–2929.
[57] M. Molina-Sabio, M.T. Gonzalez, F. Rodriguez-Reinoso, A. Sepúlveda-Escribano, Effect of steam and carbon dioxide activation in the micropore size distribution of activated carbon, Carbon 34 (4) (1996) 505–509.
[58] W. Luo, B. Wang, C.G. Heron, M.J. Allen, J. Morre, C.S. Maier, W.F. Stickle, X. Ji, Pyrolysis of cellulose under ammonia leads to nitrogen-doped nanoporous carbon generated through methane formation, Nano Lett. 14 (4) (2014) 2225–2229.
[59] J. Liang, X. Du, C. Gibson, X.W. Du, S.Z. Qiao, N-Doped graphene natively grown on hierarchical ordered porous carbon for enhanced oxygen reduction, Adv. Mater. 25 (43) (2013) 6226–6231.
[60] K.S. Park, Z. Ni, A.P. Côté, J.Y. Choi, R. Huang, F.J. Uribe-Romo, H.K. Chae, M. O'Keeffe, O.M. Yaghi, Exceptional chemical and thermal stability of zeolitic imidazolate frameworks, Proc. Natl. Acad. Sci. 103 (27) (2006) 10186–10191.
[61] A.P. Côté, A.I. Benin, N.W. Ockwig, M. O'Keeffe, A.J. Matzger, O.M. Yaghi, Porous, crystalline, covalent organic frameworks, Science 310 (5751) (2005) 1166–1170.
[62] S. Yang, X. Feng, X. Wang, K. Müllen, Graphene-based carbon nitride nanosheets as efficient metal-free electrocatalysts for oxygen reduction reactions, Angew. Chem. Int. Ed. 50 (23) (2011) 5339–5343.
[63] J.-S. Li, S.-L. Li, Y.-J. Tang, M. Han, Z.-H. Dai, J.-C. Bao, Y.-Q. Lan, Nitrogen-doped Fe/Fe 3 C@ graphitic layer/carbon nanotube hybrids derived from MOFs: efficient bifunctional electrocatalysts for ORR and OER, Chem. Commun. 51 (13) (2015) 2710–2713.
[64] J. Tang, R.R. Salunkhe, J. Liu, N.L. Torad, M. Imura, S. Furukawa, Y. Yamauchi, Thermal conversion of core-shell metal-organic frameworks: a new method for selectively functionalized nanoporous hybrid carbon, J. Am. Chem. Soc. 137 (4) (2015) 1572–1580.
[65] K. Yasuda, A. Taniguchi, T. Akita, T. Ioroi, Z. Siroma, Platinum dissolution and deposition in the polymer electrolyte membrane of a PEM fuel cell as studied by potential cycling, PCCP 8 (6) (2006) 746–752.
[66] K.-W. Nam, J. Song, K.-H. Oh, M.-J. Choo, H. Park, J.-K. Park, J. Choi, Perfluorosulfonic acid-functionalized Pt/graphene as a high-performance oxygen reduction reaction catalyst for proton exchange membrane fuel cells, J. Solid State Electrochem. 17 (3) (2013) 767–774.
[67] S. Chen, J. Duan, M. Jaroniec, S.-Z. Qiao, Nitrogen and oxygen dual-doped carbon hydrogel film as a substrate-free electrode for highly efficient oxygen evolution reaction, Adv. Mater. 26 (18) (2014) 2925–2930.